Three-dimensionally printed biological machines powered by skeletal muscle

Caroline Cvetkovic[a,b,1], Ritu Raman[b,c,1], Vincent Chan[a,b,d], Brian J. Williams[b,c], Madeline Tolish[e], Piyush Bajaj[a,b,2], Mahmut Selman Sakar[d,3], H. Harry Asada[d], M. Taher A. Saif[b,c], and Rashid Bashir[a,b,4]

[a]Department of Bioengineering, University of Illinois at Urbana–Champaign, Urbana, IL 61801; [b]Micro and Nanotechnology Laboratory, University of Illinois at Urbana–Champaign, Urbana, IL 61801; [c]Department of Mechanical Science and Engineering, University of Illinois at Urbana–Champaign, Urbana, IL 61801; [d]Department of Mechanical Engineering, Massachusetts Institute of Technology, Cambridge, MA 02139; and [e]Department of Biomedical Engineering, Vanderbilt University, Nashville, TN 37325

Combining biological components, such as cells and tissues, with soft robotics can enable the fabrication of biological machines with the ability to sense, process signals, and produce force. An intuitive demonstration of a biological machine is one that can produce motion in response to controllable external signaling. Whereas cardiac cell-driven biological actuators have been demonstrated, the requirements of these machines to respond to stimuli and exhibit controlled movement merit the use of skeletal muscle, the primary generator of actuation in animals, as a contractile power source. Here, we report the development of 3D printed hydrogel "bio-bots" with an asymmetric physical design and powered by the actuation of an engineered mammalian skeletal muscle strip to result in net locomotion of the bio-bot. Geometric design and material properties of the hydrogel bio-bots were optimized using stereolithographic 3D printing, and the effect of collagen I and fibrin extracellular matrix proteins and insulin-like growth factor 1 on the force production of engineered skeletal muscle was characterized. Electrical stimulation triggered contraction of cells in the muscle strip and net locomotion of the bio-bot with a maximum velocity of ~156 μm s^{-1}, which is over 1.5 body lengths per min. Modeling and simulation were used to understand both the effect of different design parameters on the bio-bot and the mechanism of motion. This demonstration advances the goal of realizing forward-engineered integrated cellular machines and systems, which can have a myriad array of applications in drug screening, programmable tissue engineering, drug delivery, and biomimetic machine design.

bioactuator | stereolithography

Soft robotic devices composed of adaptable materials permit deformation, locomotion, and control with greater degrees of freedom in a simple, low-power, and cost-effective manner compared with traditional robotics composed of metallic and rigid structures (1–3). Combining biological entities such as cells or tissues with soft materials can yield biological machines with the ability to dynamically sense and adapt to environmental cues and applied stimuli. A biointegrated approach to soft robotics can allow for the realization of biological machines with the ability to interface with the environment and other living systems. An intuitive demonstration of a biological machine is a system that can generate force resulting in net locomotion. To that end, many studies have explored the use of biological components, such as DNA (4), swarms of bacterial cells (5), motile sperm cells (6), and contractile muscular tissues excised from living organisms (7–9) as power sources with the ability to exhibit a dynamic locomotive response across length scales (10–13).

Recent advances in cardiac muscle tissue engineering have yielded dense tissues that form a syncytium, enabling the coordinated propagation of electrical signals and synchronous contraction of engineered muscle (14). This advantageous property has helped to produce machines that include self-assembling microelectromechanical-system-based cantilevers (15), 2D biohybrid "muscular thin films" (16), and "crab-like" robots

(17). These systems were powered by applied electric field stimulation or spontaneous contraction of engineered cardiac muscle, which have also been used as power sources for locomotive machines such as a swimming muscle-elastomer "jellyfish" (18), a self-propelled swimming robot (19), and a walking millimeter-scale "biological bimorph" cantilever (20, 21), respectively.

Although these soft robots have used cardiac muscle, it should be noted that skeletal muscle is the primary generator of actuation in animals. In vivo, skeletal muscle exhibits organized modular tissue architecture on a range of length scales and supports uniaxial force production. Unlike cardiac tissue, it does not demonstrate significant spontaneous contractility, allowing for more precise control over actuation via external signaling from sources such as electrical stimulation, neural signals, or optogenetics (22). Furthermore, skeletal muscle can interface with multiple other mammalian cell types, such as neurons and endothelial cells, making it an ideal platform for producing locomotion in living cellular systems (11, 12, 23).

In this paper, we present an untethered locomotive biological machine, or "bio-bot," powered by the contraction of engineered skeletal muscle. The structure of the bio-bot was fabricated from a synthetic hydrogel using stereolithographic 3D printing, which boasts a short fabrication time, potential for scalability, and

Significance

Cell-based soft robotic devices could have a transformative impact on our ability to design machines and systems that can dynamically sense and respond to a range of complex environmental signals. We demonstrate innovative advancements in biomaterials, tissue engineering, and 3D printing, as well as an integration of these technologies, to forward engineer a controllable centimeter-scale biological machine capable of locomotion on a surface in fluid. Due in part to their elastic nature and the living components that can permit a dynamic response to environmental and applied stimuli, these biological machines can have diverse applications and represent a significant advancement toward high-level functional control over soft biorobotic systems.

spatial control. The use of additive manufacturing processes for a myriad of biomedical applications has increased in recent years, owing to the user's ability to rapidly polymerize an assortment of biocompatible materials with controllable geometric and mechanical properties at the micro- and macroscales (24). Skeletal muscle myoblasts were embedded in a natural extracellular matrix (ECM) of collagen I and fibrin matrix proteins, differentiated in the presence of insulin-like growth factor 1 (IGF-1), and self-assembled into a 3D muscle strip capable of contractility and sufficient force generation to power net locomotion of the bio-bot upon electrical signaling (Fig. S1). To our knowledge, this is the first demonstration of an untethered biological machine powered by engineered mammalian skeletal muscle and controlled purely via external signaling, and hence represents an important advance in building biointegrated soft robotic devices for a myriad array of applications in sensing and actuation.

Results and Discussion

Design and Fabrication of 3D Bio-bots. To construct the structure of the bio-bot, we used a modified stereolithography apparatus (SLA), a liquid-based rapid prototyping technology (24), to print a millimeter-scale hydrogel poly(ethylene glycol) diacrylate of M_r 700 g mol^{-1} (PEGDA M_r 700) device composed of two stiff pillars connected by a compliant beam (Fig. 1 A and B). We used a linear elastic simulation to determine optimal beam and pillar dimensions that would combine high deflection with a robust mechanical structure (Fig. S2). A liquid suspension of mouse myoblast cell line C2C12 skeletal muscle myoblasts and ECM proteins was added around the pillars of the bio-bot and polymerized via gelation of the matrix proteins (Fig. 1 C and D). Embedded cells exerted traction forces on the fibrous proteins via integrin attachments to compact the matrix into a 3D muscle strip over time (Fig. S3 D and E and Movie S1), and the capped pillars acted as a physical anchor for the muscle strip. This bio-inspired design mimics the in vivo musculoskeletal arrangement in which force transmission occurs from a contracting muscle to bone through a connecting tendon (Fig S3F).
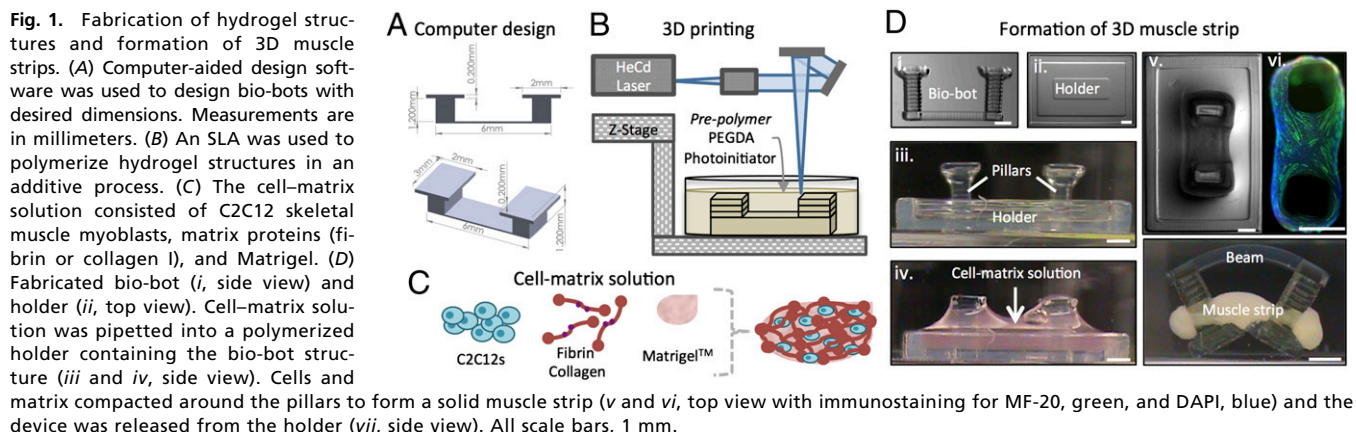
The ECM contributes to maintaining cellular processes and communication in normal growth and maturation of skeletal myoblasts. Collagen I and fibrin are natural hydrogels that allow for muscle cell proliferation, spreading, and alignment, as well as tissue contraction on a macroscopic scale (25, 26). We tested both matrix proteins for their ability to support the development and organization of embedded myoblasts and provide a compliant system for tissue contraction. The cell–matrix solution consisted of either matrix protein with cell concentrations varying from $1–10 \times 10^6$ cells ml^{-1} (Fig. S4). We observed that cell traction forces increased with cell concentrations; lower concentrations resulted in less compaction, whereas higher cell concentrations caused muscle strip fracture. We deemed an intermediate concentration of 5×10^6 cells ml^{-1} as optimal.
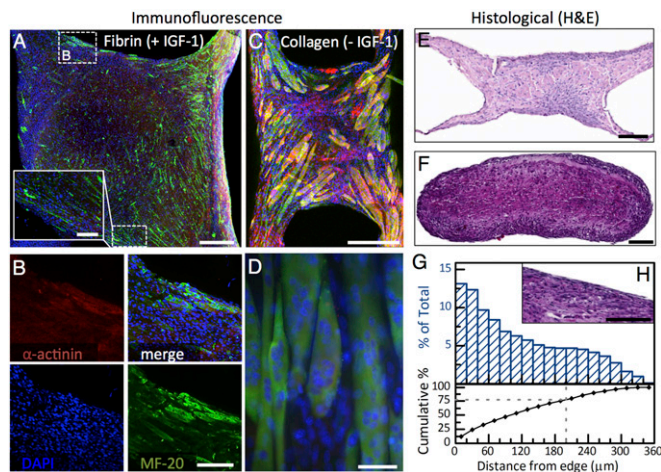
Muscle Strip Differentiation and Robustness. To improve the formation and functional performance of 3D muscle strips, we studied the effect of IGF-1 on myotube formation in 2D and 3D culture. IGFs play a role in skeletal tissue growth in vertebrates by encouraging myoblast proliferation and differentiation (27, 28). Overexpression or exogenous addition of IGF-1 also enhances muscle hypertrophy (29) and decelerates muscle decline in differentiated myofibers (30). In 2D culture, as expected, the fusion of myoblast precursor cells during myogenesis produced elongated, multinucleated myotubes (31). Over 2.5 wk, the average myotube density of myoblast cultures supplemented with 50 ng ml^{-1} IGF-1 significantly increased from $31.8 \pm 8.3–126.9 \pm 30.3$ myotubes mm^{-2} compared with the control with no added IGF-1 (Fig. S5 A and B), and did not change significantly after day 7, when muscle strips were electrically stimulated.

Translating these results to 3D, we then studied the effect of IGF-1 addition (beyond that included in the Matrigel basement membrane) on the formation and functionality of fibrin and collagen muscle strips. Differentiated, multinucleated myotubes were distributed throughout muscle strips supplemented with IGF-1 (Fig. 2 A and B). Muscle strips cultured without IGF-1 contained populations of both undifferentiated myoblasts as well as multinucleated myotubes at later time points (Fig. 2 C and D), signaling that although IGF-1 increased the rate of fusion and maturation, its absence did not hinder muscle strip development. With the addition of 50 ng ml^{-1} IGF-1, the portion of the fibrin-based muscle strip occupied by cells significantly increased (Fig. S5 D and E).

Despite cross-linking during polymerization, fibrinogen is extremely susceptible to rapid degradation by cell-secreted proteases such as plasmin (32). In vivo, natural inhibitors of plasmin prevent indiscriminate matrix digestion; however, in vitro, C2C12s can produce plasmin-activating plasminogen, and a protease inhibitor such as ε-aminocaproic acid (ACA) must be added to ensure stability of the system (33). Addition of 1 mg ml^{-1} ACA helped to maintain the structural integrity of the muscle strip, significantly increasing the lifetime of the muscle strip before rupture (Fig. S5C). The bio-bots presented in this study were supplemented with 1 mg ml^{-1} ACA, and 0 (without) or 50 (with) ng ml^{-1} IGF-1.

Hematoxylin and eosin (H&E) staining of histological sections of IGF-1–supplemented fibrin muscle strips revealed an increased peripheral cell density compared with the center (Fig. 2 E–H). We located over 75% of cells within 200 μm of the edge of the fibrin muscle strip, a distance consistent with the upper limit of diffusion of oxygen within a tissue (34). Finally, we used a colorimetric assay to evaluate cell viability over time. The relative absorbance of muscle strips (normalized to day 0) indicated a $85.76 \pm 10.74\%$ and $79.71 \pm 14.78\%$ viability of cells within the muscle strip after days 6 and 9, respectively (Fig. S5F). Compared with the control muscle strips on day 9, the IGF-1-supplemented muscle strips demonstrated enhanced cell proliferation.

Fig. 1. Fabrication of hydrogel structures and formation of 3D muscle strips. (A) Computer-aided design software was used to design bio-bots with desired dimensions. Measurements are in millimeters. (B) An SLA was used to polymerize hydrogel structures in an additive process. (C) The cell–matrix solution consisted of C2C12 skeletal muscle myoblasts, matrix proteins (fibrin or collagen I), and Matrigel. (D) Fabricated bio-bot (i, side view) and holder (ii, top view). Cell–matrix solution was pipetted into a polymerized holder containing the bio-bot structure (iii and iv, side view). Cells and matrix compacted around the pillars to form a solid muscle strip (v and vi, top view with immunostaining for MF-20, green, and DAPI, blue) and the device was released from the holder (vii, side view). All scale bars, 1 mm.

Fig. 2. Biological characterization of muscle strips. (*A*) Longitudinal fibrin muscle strip slice (day 9). Scale bar, 500 μm. (*Inset*) Scale bar, 200 μm. (*B*) Myotubes aligned along the fibrin muscle strip perimeter. Scale bar, 200 μm. (*C*) Longitudinal collagen muscle strip slice (day 14). Scale bar, 500 μm. (*D*) Multinucleated myotubes in the collagen muscle strip. Scale bar, 50 μm. (*E–H*) H&E staining of fibrin muscle strip sections (day 9). All scale bars, 200 μm. (*E*) Longitudinal and (*F*) transverse muscle strip sections. (*G*) Quantitative analysis of transverse sections demonstrated 75% of cells within 200 μm from the edge (*n* = 8). (*H*) Perimeter of transverse section of the muscle strip.

Optimization of Muscle Force Generation. To optimize force production capabilities of the engineered muscle strip, we studied the effect of varying biological and mechanical environmental cues during muscle differentiation and maturation. By varying the laser energy dose of polymerization of the SLA, we created hydrogel structures with a range of tunable properties and conformations without changing the composition or molecular weight of the material. The elastic modulus of the hydrogel beam (as measured by tensile testing in a hydrated sample chamber) increased logarithmically from 214.6–741.6 kPa with laser energy doses varying from 108.7–512.6 mJ cm^{-2}, due to a higher degree of cross-linking by higher energy doses. With compaction of the muscle strip, traction forces exerted by cells produced an inward force on the pillars, which gave rise to varying degrees of bending in the beam. As expected, the stiffer hydrogel structures offered a greater resistance to bending; thus, beams with higher elastic moduli exhibited a lower deflection in response to passive tension forces exerted by the muscle strips (Fig. 3*A* and Fig. S6*A*).

Using Euler–Bernoulli linear bending theory (*SI Methods* and Fig. S6*C*), we derived a formula relating the observed hydrogel beam deflection to the muscle-generated passive tension force. An increase in beam stiffness resulted in an increased tension in the muscle strip at rest. For elastic moduli of 214.6, 319.4, 411.2, and 489.3 kPa, the passive tension averaged 860.6 ± 47.2, 992.7 ± 34.3, 1,103.6 ± 45.8, and 1,146.0 ± 69.0 μN, respectively, in fibrin-based muscle strips cultured with IGF-1. We then used finite-element analysis software (ANSYS) to model and simulate global displacement of the beam and pillars in response to an applied force (Fig. 3 *C* and *D*). The simulated deflection values differed 18–19% from actual measurements (Fig. S6*D*), validating our methods to extract passive tension and predict muscle force output.

The bio-bot pillars provided uniaxial constraint for cell alignment during compaction, allowing the myotubes to mature in a macroenvironment that mimics the native organization of functional skeletal muscle. The increase in passive tension generated by the muscle strip with increasing hydrogel stiffness indicated that the forces exerted by cells could be modified in relation to mechanical environment of the muscle. Others have validated an increase in force output with dynamic mechanical stimulation (35); here, we also demonstrate that a static mechanical cue imposed

during muscle development contributes to improved functionality, providing further evidence that many types of mechanical stresses are required for muscle development (36). Bio-bot hydrogel structures with a beam stiffness of 319.4 kPa were selected for subsequent experiments, as they combined the advantages of sufficiently high passive tension forces with deformable structures suitable for locomotion.

To determine an optimal matrix system for engineered muscle functionality, we compared the passive tension forces generated by collagen- and fibrin-based cell–matrix systems. In muscle strips containing the same number of cells, we observed a significant increase in passive tension in those containing fibrin (629.3 ± 8.2 μN) compared with collagen (534.2 ± 5.8 μN) (Fig. S6*E*). Advantageously, fibrin polymerizes relatively quickly compared with other ECM proteins, and it can undergo large deformations without breaking (37, 38). The ability to sustain large strains while maintaining structural integrity during muscle contraction was a necessary characteristic for applications in bioactuation.

Examining the effect of varying other biological environmental cues, we observed that fibrin-based muscle strips supplemented with IGF-1 demonstrated a 70.7% increase in passive tension force, from 581.4 ± 20.6–992.7 ± 34.3 μN (*P* < 0.001, *n* = 4), compared with the control without IGF-1. We attributed this significant increase in force production to a greater number of differentiated myotubes in muscle strips supplemented with IGF-1, an observation confirmed by immunostaining and other reported variations of 3D engineered muscle constructs (39). We calculated a normalized stress in the muscle strips with IGF-1 by dividing the passive tension by the cross-sectional area of the tissue, which averaged 1.2 ± 0.04 mm^2 (*n* = 9, Fig. S6*F*). The passive stress in the muscle strips averaged 0.84 ± 0.03 kPa, values that are comparable to those of similar muscle-based 3D cell–matrix systems with collagen or fibrin (22, 26, 40, 41).

Electrically Paced Actuation of Bio-bots. To externally control muscle contraction and bio-bot locomotion, we used a custom-designed setup (42) to stimulate reproducible contraction of
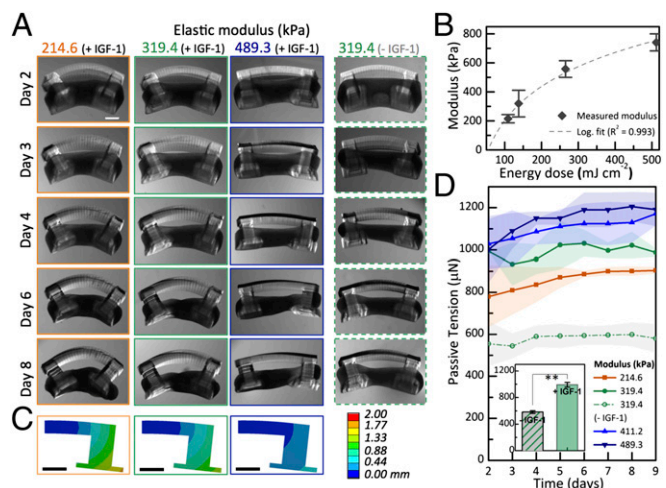
Fig. 3. Analysis of bending and passive tension. (*A*) Over time, bio-bot beams polymerized with varying energy doses exhibited different bending profiles. Scale bar, 1 mm. (*B*) Elastic modulus of the beam as a function of energy dose (R^2 > 0.99, *n* = 5). Increasing polymerization energy resulted in a higher modulus and less bending. (*C*) Finite-element analysis simulation demonstrating global deflection of the bio-bot beam and pillars on day 8. (*D*) Passive tension in the muscle strip as a function of time, modulus, and addition of IGF-1 (*n* = 3, 489.3 kPa; *n* = 4, others). Increasing beam stiffness resulted in a higher muscle strip tension. (*Inset*) Addition of IGF-1 significantly increased the average tension by 70.7% (for 319.4-kPa stiffness) over time period shown. Statistics represent one-way ANOVA and Tukey's test, with ** = *P* < 0.001. All data are presented as mean ± SD (shaded region in *D*).

excitable cells within the muscle strip with a bipolar electrical pulse train (Fig. 4A and Fig. S7). By mimicking signals necessary for the generation of an action potential in vivo, electrical pulse stimulation can induce protein expression, contractile ability, cell alignment, and differentiation of skeletal muscle in vitro (43–46); here, we harnessed the stimulation to coordinate contraction of multiple myotubes within the muscle strip, which collectively generated sufficient force to visibly deform the hydrogel structure of the bio-bot. Fibrin-based muscle strips supplemented with IGF-1 and stimulated at constant frequencies of 1, 2, or 4 Hz demonstrated a consistent output of 1.01 ± 0.003, 2.01 ± 0.01, and 3.95 ± 0.05 contractions s^{-1}, respectively ($n = 10$, Fig. 4B, Movies S2 and S3), establishing that the bio-bots could be reliably paced with this method. We witnessed twitch contractions below 8–10 Hz and tetanus above this upper frequency limit. In contrast, non-IGF-1-supplemented muscle strips did not respond to stimulation during this time period, a result attributed to fewer myotubes. We predict a response at later time points, as others have shown electrically induced contractility of C2C12s or primary cells in 3D tissue constructs after 14 d (and sometimes up to 30+ d) following formation (26, 47–50). However, IGF-1 treatment presents a simple and physiologically relevant method to enhance differentiation for functional output via electrical stimulation on a shorter time scale (here, as early as day 7). Additionally, we observed that the range of active tension remained above 99.3% of the initial value during 8 min of electrical stimulation at hour 0, and above 98.8% of the initial value at hour 6, revealing a consistent force output from the engineered muscle strips both within a constant stimulation period and at later time points (Fig. S8A).

A Kelvin–Voigt viscoelasticity model that correlated the observed cyclic displacement to the contractile force was used to extract the active tension generated by IGF-1-supplemented muscle strips in response to electrical stimulation (Fig. 4C). The range of active tension during contraction decreased with increasing stimulation frequency, from a dynamic fluctuation of 198.68 μN during 1-Hz stimulation to 109.48 μN during 4-Hz stimulation (Fig. 4D). The active tension data followed a positive force–frequency relationship in which the magnitude of the active tension exerted by the muscle increased, even while the range of pillar motion decreased. Furthermore, as a consequence of muscle relaxation times exceeding the period between electrical pulses at higher frequencies, we observed a temporal summation of force that resulted in a baseline tension increase over time. The muscle strips therefore displayed functional behavior characteristic to physiological skeletal muscle, in which force output increases with frequency before reaching tetanus (11).

Demonstration of Controlled Directional Movement. We aimed to create a biomimetic "crawling" mechanism reminiscent of an inchworm's movement. Using finite-element simulations, we explored a symmetric and an asymmetric design for the bio-bots (Fig. 5A). For the asymmetric design, we extended the length of one pillar of the bio-bot hydrogel structure, allowing for asymmetric bending of the flexible beam (Fig. S3A), hypothesizing that the introduction of deliberate asymmetry within the structure would increase the moment arm between the muscle strip anchor point and the beam, as well as the range of motion between pillars during displacement. It would also change the contact area of the base to the surface for one pillar versus the other. These simulations revealed that as expected, the symmetric structure did not demonstrate significant locomotion. However, an asymmetric structure exhibited nonuniform distribution of stress in the hydrogel structure in response to muscle contraction, corresponding to asymmetric pillar displacements (Fig. 5A and Movies S4 and S5). Simulations revealed that asymmetric actuation and force generation of the muscle strips by geometric design of the bio-bot would produce greater net displacement over a fixed time and create a more efficient and predictable locomotive mechanism compared with the symmetric design.

Consistent with the simulation results, we experimentally observed that for a symmetric hydrogel structure, electrical pacing of skeletal muscle strips attached to bio-bot structures either did not result in net locomotion of the bio-bot across a substrate, or in some cases, resulted in a very small locomotion (Fig. 5B and Movie S6). Because the hydrogel structure itself was symmetric, we hypothesized that any observed small locomotion of the symmetric structure was attributed to asymmetry in muscle strip formation and force distribution. From a top-view movie, we tracked bio-bot pillar displacements in response to muscle contractions over time and observed that when both pillars displaced equally, the bio-bot did not move. Interestingly, for the minimally locomotive bio-bots, when one pillar displaced more than the other (Fig. 5C), the bio-bot always "crawled" in the direction of the pillar that demonstrated greater displacement in response to muscle contraction. For the case of these symmetric devices, these small velocities were found to be less than 4.34 μm s^{-1} at electrical stimulation of 1-Hz frequency (Fig. 5D).

We found that muscle strips coupled to the asymmetric compliant hydrogel structure drove inchworm-like crawling locomotion with maximum velocity. Contraction of muscle strips on asymmetric bio-bots resulted in a maximum velocity of 117.8 μm s^{-1} in response to electrical stimulation of 1-Hz frequency, an increase in velocity of more than 25-fold compared with the symmetric design (Fig. 5 E–G, Fig. S8, and Movie S7). During electrically paced locomotion, the asymmetric bio-bot produced an active tension force of 394.7 ± 56.6 μN, or 27.9% of the maximum force (Fig. 5G).

Although bio-bot pillar displacement decreased with increasing stimulation frequency, the observed increase in force generation led us to test the effect of stimulation frequency on bio-bot locomotion. The increased number of contractions with increasing stimulation frequency within a given time period resulted in an increased average velocity of the asymmetric bio-bot, which was measured to be 117.8, 132.2, and 156.1 μm s^{-1} at 1, 2, and 4 Hz, respectively, during the time period shown (Fig. 5H and Movie S8). At all frequencies, the asymmetric bio-bot moved in the direction of the pillar that demonstrated greater displacement, as predicted (Fig. S8C).
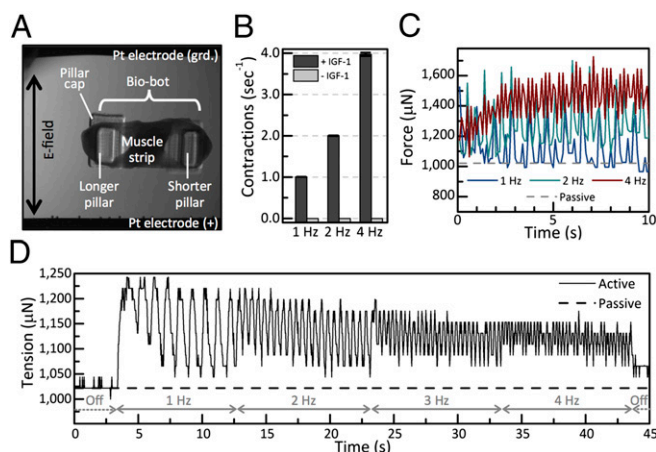
Fig. 4. Electrical control and pacing. (A) During stimulation, bio-bots were placed standing up on the surface of the dish, with the muscle strip's longitudinal axis parallel to the electrodes and perpendicular to the applied field. (B) IGF-1-supplemented bio-bots were reliably paced at stimulation frequencies of 1, 2, or 4 Hz. Bio-bots not supplemented with IGF-1 did not respond to stimulation at any frequency in the observed time period. (C) A Kelvin–Voigt viscoelasticity model was used to extract active tension generated by the muscle strip in response to electrical stimulation. (D) Muscle strip time-varying active tension was calculated for a bio-bot undergoing varying electrical stimulation (0, 1, 2, 3, 4, 0 Hz) during one experiment, and followed a positive force–frequency relationship.
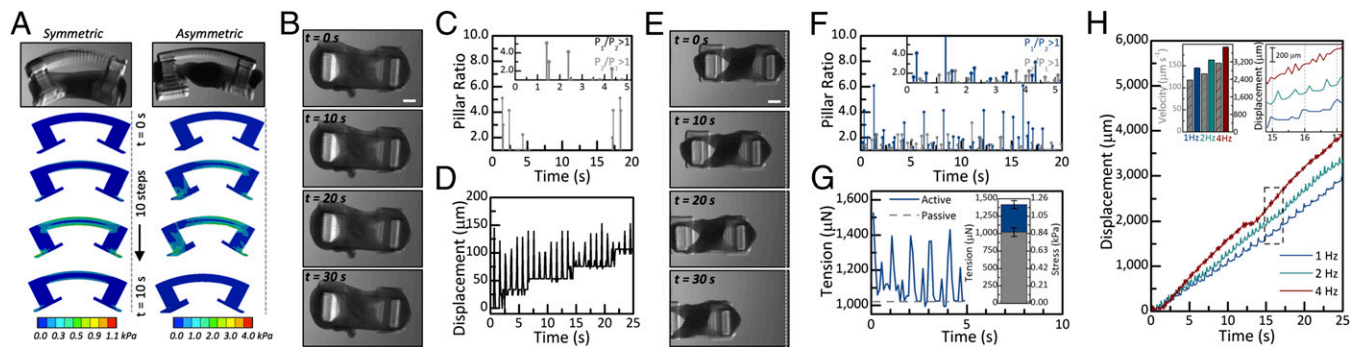
Fig. 5. Simulation and movement profiles of symmetric and asymmetric bio-bots supplemented with IGF-1. (*A*) von Mises stress of a symmetric and asymmetric bio-bot. The range of one contraction is shown over a period of 10 s (10 "steps" at 1-Hz stimulation). (*B* and *E*). Top-view time-lapse images of the symmetric (*B*) and asymmetric (*E*) bio-bot's movement. All scale bars, 1 mm. (*C* and *F*) Relative ratios of pillar movement over time during 1-Hz stimulation. The bio-bots moved in the direction of greater pillar movement during contraction. (*D*) Displacement (μm) of a symmetric bio-bot at 1-Hz stimulation during a 25-s interval when contraction produced maximum displacement along the surface. (*G*) Active tension force of the asymmetric bio-bot during locomotion. (*H*) The increased number of contractions with increasing stimulation frequency within a given time period resulted in an increased average velocity of the asymmetric bio-bot. (*Inset, Left*) Velocity (gray) and total displacement. (*Inset, Right*) Zoom of boxed region.

Conclusions

Soft robotic devices integrated with biological systems combine the advantages of high-degree-of-freedom compliant response with dynamic sensing and actuation capabilities. We report the design and fabrication of a skeletal muscle powered machine that can be controlled and paced via external signaling, instead of relying on spontaneous muscle contraction. Modeling and simulations were used to study the effect of changing design parameters on functional response, resulting in a more comprehensive picture of the locomotive mechanisms. We improved the force generation capacity and functional performance of this engineered tissue by differentiating muscle strips in an optimized fibrin-based ECM environment supplemented with IGF-1 growth factor. Muscle strips displayed a tunable functional response in relation to the static stress imposed by a 3D printed hydrogel structure, mimicking the in vivo mechanical environment of muscle maturation. Finally, electrical stimulation triggered contraction of engineered muscle, driving a biomimetic and controllable directional locomotion.

Although other studies have explored the use of excised and engineered biological components such as cardiac muscle tissues for applications in bioactuation, these studies lack a fabrication methodology that offers flexibility in precisely specifying geometric, material, and biological component design parameters (Fig. S9). Our stereolithographic 3D-printing-based biofabrication system supports the integration of a variety of scaffolding materials and multiple cell types, representing a significant advancement toward engineering biological machines capable of complex and controllable functional behaviors. Furthermore, our biofabrication methodology can readily be modified to demonstrate other mechanisms of locomotion and force output (such as swimming and pumping) while also creating a platform for future studies integrating different biomaterials and cell types. The incorporation of motor neurons resulting in neuromuscular junction formation would lead to more complex mechanisms of functional control of the engineered muscle. Additionally, integration of endothelial cells to engineer an internal vasculature would increase diffusion of nutrients and oxygen to the muscle tissue, thereby increasing efficiency and long-term viability of a living biological machine.

Forward engineering of biological machines can help to advance the understanding of the fundamental scientific and design principles underlying living systems and lead to a quantitative understanding of the way integrated cellular systems sense and respond to environmental signals (1). In the long term, we envision that this system could serve as a basis for target applications such as microscale tissue fabrication for drug screening and tissue- and organ-on-a-chip mimics, dynamic biocompatible microelectronics

and medical implants, and forward-engineered biological machines and systems.

Methods

Design and Fabrication of Parts. A commercial SLA (250/50, 3D Systems) was modified for polymerization as previously described (20, 51). Parts generated using computer-aided design software were exported to 3D Lightyear software (v1.4, 3D Systems), which sliced the part into layers. Prepolymer solutions for bio-bots and holders are described in *SI Methods*. For fabrication of bio-bots, an 18 × 18-mm-square cover glass was secured to the center of a 35-mm culture dish (both with hydrophilic surfaces) before fabrication. For bio-bot holders, cover glass slides were first treated with 2% (vol/vol) 3-(trimethoxysilyl)propyl methacrylate (Sigma-Aldrich) in 200-proof ethanol (100% EtOH) for 5 min and then washed in 100% EtOH for 3 min, dried, and secured to the center of a 35-mm dish. Following fabrication, each structure was rinsed in PBS, sterilized in 70% EtOH for 1 h, and allowed to reswell in PBS for at least 1 h.

Mechanical Testing. To characterize the mechanical properties of PEGDA M_r 700, dogbone-shaped test specimens fabricated with the SLA were superglued to stainless steel bars, then fixed in custom-fabricated structures in a hydrated sample chamber (*SI Methods*). An ElectroForce BioDynamic test instrument (5100, Bose) with a 1,000-g load cell applied uniaxial tension at each end of the structure at 0.05 mm s^{-1} (Fig. S6B). Control software (Wintest) was used to track load, displacement, and strain ε. Elastic modulus E was determined from the linear portion of stress–strain curves.

Cell Culture and Formation of Muscle Strip. C2C12 murine myoblasts were transfected with pAAV-Cag-Chr2-GFP-2A-Puro plasmid to express ChR2 (22). Cells were maintained in growth medium (GM) or differentiation medium (DM) as described in *SI Methods*. During cell seeding, C2C12s suspended in GM were mixed with an ice-cold liquid solution of Matrigel basement membrane matrix and type I collagen or fibrin, as detailed in *SI Methods*, and added to each holder. After 24 h, bio-bots were cultured in DM with antifibrinolytic 6-ACA and human IGF-1 (both Sigma-Aldrich) as noted.

Beam Deflection and Muscle Strip Passive Tension. Side-view images of symmetric bio-bots were taken every 24 h using a stereomicroscope (MZ FL III, Leica Microsystems) with a digital microscope camera (Flex, SPOT Imaging Solutions). To model bio-bot deformation in the passive (bent but unmoving) state, designs was reconstructed using SolidWorks and imported into ANSYS. Appropriate material properties were assigned and a force equal to the calculated passive tension was applied to the base at a distance specified by the measured moment arm. Resultant solutions of total deformation were examined to find maximum beam deflection. Passive tension in the muscle strip was determined using Euler–Bernoulli linear beam theory (*SI Methods*). Stress was calculated by dividing the tension by the muscle strip's cross-sectional area A, determined from transverse H&E sections.

Electrical Stimulation. A custom-designed electrical setup was built as previously described (42) (Fig. S7). Bio-bots were stimulated with bipolar electrical pulses of 20-V amplitude (21.6-V cm^{-1} field strength) and 50-ms pulse width. Top-view movies were acquired with a stereomicroscope with a digital microscope camera at 9.2 frames per second (fps). Side-view movies were acquired using a camcorder (Handycam DCR-SR65, Sony) at 30 fps. Electrodes were sterilized in 70% EtOH and rinsed with PBS between experiments.

Characterization of Movement and Force. Active tension exerted by contracting muscle strips upon electrical stimulation was calculated by treating the bio-bot structure as a viscoelastic body governed by a Kelvin–Voigt model (*SI Methods*). An automated MATLAB script was designed to track the location of a user-specified feature with a normalized 2D cross-correlation and provided X–Y coordinates of a specific point on the bio-bot for each frame. This software tracked the distance between the longer and shorter pillar caps during stimulation from a top-view movie (Fig. S8E). Frequency was measured by manually counting contractions in identical time segments.

Immunofluorescence and Histology. Muscle strips were removed from bio-bot pillars and prepared for immunostaining for myosin heavy chain, sarcomeric α-actinin, and 4′,6-diamindino-2-phenylindole (DAPI), or histological staining with H&E (*SI Methods*). Muscle strips were imaged with a confocal microscope (LSM 710, Zeiss) or inverted fluorescent microscope (IX81, Olympus). Image stacks were processed using Zen software (2010, Zeiss) and ImageJ.

Statistical Analysis. Results are presented as mean ± SD. All statistical analyses were performed with OriginPro software and represent one-way ANOVA followed by Tukey's Multiple Comparison Test for $P < 0.001$, $P < 0.01$, or $P < 0.05$ as noted.

1. Kovač M (2013) The bioinspiration design paradigm: A perspective for soft robotics. *Soft Robot* 1(1):28–37.
2. Majidi C (2013) Soft robotics: A perspective—current trends and prospects for the future. *Soft Robot* 1(1):5–11.
3. Shepherd RF, et al. (2011) Multigait soft robot. *Proc Natl Acad Sci USA* 108(51):20400–20403.
4. Yurke B, Turberfield AJ, Mills AP, Jr., Simmel FC, Neumann JL (2000) A DNA-fuelled molecular machine made of DNA. *Nature* 406(6796):605–608.
5. Martel S, Tremblay CC, Ngakeng S, Langlois G (2006) Controlled manipulation and actuation of micro-objects with magnetotactic bacteria. *Appl Phys Lett* 89:233904.
6. Magdanz V, Sanchez S, Schmidt OG (2013) Development of a sperm-flagella driven micro-bio-robot. *Adv Mater* 25(45):6581–6588.
7. Herr H, Dennis RG (2004) A swimming robot actuated by living muscle tissue. *J Neuroeng Rehabil* 1(1):6.
8. Akiyama Y, et al. (2013) Atmospheric-operable bioactuator powered by insect muscle packaged with medium. *Lab Chip* 13(24):4870–4880.
9. Akiyama Y, Hoshino T, Iwabuchi K, Morishima K (2012) Room temperature operable autonomously moving bio-microrobot powered by insect dorsal vessel tissue. *PLoS ONE* 7(7):e38274.
10. Dennis RG, Herr H (2005) *Biomimetics: Biologically Inspired Technologies*, ed Bar-Cohen Y (CRC, Boca Raton, FL), 1st Ed, pp 243–266.
11. King AM, Loiselle DS, Kohl P (2004) Force generation for locomotion of vertebrates: Skeletal muscle overview. *IEEE J Oceanic Eng* 29(3):684–691.
12. Duffy RM, Feinberg AW (2014) Engineered skeletal muscle tissue for soft robotics: Fabrication strategies, current applications, and future challenges. *Wiley Interdiscip Nanomed Nanobiotechnol* 6(2):178–195.
13. Chan V, Asada HH, Bashir R (2014) Utilization and control of bioactuators across multiple length scales. *Lab Chip* 14(4):653–670.
14. Vunjak-Novakovic G, et al. (2010) Challenges in cardiac tissue engineering. *Tissue Eng Part B Rev* 16(2):169–187.
15. Xi J, Schmidt JJ, Montemagno CD (2005) Self-assembled microdevices driven by muscle. *Nat Mater* 4(2):180–184.
16. Feinberg AW, et al. (2007) Muscular thin films for building actuators and powering devices. *Science* 317(5843):1366–1370.
17. Kim J, et al. (2007) Establishment of a fabrication method for a long-term actuated hybrid cell robot. *Lab Chip* 7(11):1504–1508.
18. Nawroth JC, et al. (2012) A tissue-engineered jellyfish with biomimetic propulsion. *Nat Biotechnol* 30(8):792–797.
19. Williams BJ, Anand SV, Rajagopalan J, Saif MTA (2014) A self-propelled biohybrid swimmer at low Reynolds number. *Nat Commun* 5:3081.
20. Chan V, et al. (2012) Development of miniaturized walking biological machines. *Sci Rep* 2:857.
21. Chan V, et al. (2012) Multi-material bio-fabrication of hydrogel cantilevers and actuators with stereolithography. *Lab Chip* 12(1):88–98.
22. Sakar MS, et al. (2012) Formation and optogenetic control of engineered 3D skeletal muscle bioactuators. *Lab Chip* 12(23):4976–4985.
23. Lieber RL (2002) *Skeletal Muscle Structure, Function, & Plasticity*, ed Julet T (Lippincott Williams & Wilkins, Baltimore), 2nd Ed.
24. Melchels FPW, Feijen J, Grijpma DW (2010) A review on stereolithography and its applications in biomedical engineering. *Biomaterials* 31(24):6121–6130.
25. Bian W, Bursac N (2008) Tissue engineering of functional skeletal muscle: Challenges and recent advances. *IEEE Eng Med Biol Mag* 27(5):109–113.
26. Hinds S, Bian W, Dennis RG, Bursac N (2011) The role of extracellular matrix composition in structure and function of bioengineered skeletal muscle. *Biomaterials* 32(14):3575–3583.
27. Duan C, Ren H, Gao S (2010) Insulin-like growth factors (IGFs), IGF receptors, and IGF-binding proteins: Roles in skeletal muscle growth and differentiation. *Gen Comp Endocrinol* 167(3):344–351.
28. Florini JR, Ewton DZ, Coolican SA (1996) Growth hormone and the insulin-like growth factor system in myogenesis. *Endocr Rev* 17(5):481–517.
29. Vandenburgh HH, Karlisch P, Shansky J, Feldstein R (1991) Insulin and IGF-I induce pronounced hypertrophy of skeletal myofibers in tissue culture. *Am J Physiol* 260(3 Pt 1):C475–C484.
30. Barton-Davis ER, Shoturma DI, Musaro A, Rosenthal N, Sweeney HL (1998) Viral mediated expression of insulin-like growth factor I blocks the aging-related loss of skeletal muscle function. *Proc Natl Acad Sci USA* 95(26):15603–15607.
31. Miller JB, Schaefer L, Dominov JA (1999) Seeking muscle stem cells. *Curr Top Dev Biol* 43:191–219.
32. Prentice CRM (1980) Basis of antifibrinolytic therapy. *J Clin Pathol Suppl (R Coll Pathol)* 14:35–40.
33. Kupcsik L, Alini M, Stoddart MJ (2009) Epsilon-aminocaproic acid is a useful fibrin degradation inhibitor for cartilage tissue engineering. *Tissue Eng Part A* 15(8):2309–2313.
34. Novosel EC, Kleinhans C, Kluger PJ (2011) Vascularization is the key challenge in tissue engineering. *Adv Drug Deliv Rev* 63(4-5):300–311.
35. Powell CA, Smiley BL, Mills J, Vandenburgh HH (2002) Mechanical stimulation improves tissue-engineered human skeletal muscle. *Am J Physiol Cell Physiol* 283(5):C1557–C1565.
36. Goldspink G, et al. (1992) Gene expression in skeletal muscle in response to stretch and force generation. *Am J Physiol* 262(3 Pt 2):R356–R363.
37. Liu W, et al. (2006) Fibrin fibers have extraordinary extensibility and elasticity. *Science* 313(5787):634.
38. Janmey PA, Winer JP, Weisel JW (2009) Fibrin gels and their clinical and bioengineering applications. *J R Soc Interface* 6(30):1–10.
39. Huang Y-C, Dennis RG, Larkin L, Baar K (2005) Rapid formation of functional muscle in vitro using fibrin gels. *J Appl Physiol (1985)* 98(2):706–713.
40. Boudou T, et al. (2012) A microfabricated platform to measure and manipulate the mechanics of engineered cardiac microtissues. *Tissue Eng Part A* 18(9-10):910–919.
41. West AR, et al. (2013) Development and characterization of a 3D multicell microtissue culture model of airway smooth muscle. *Am J Physiol Lung Cell Mol Physiol* 304(1):L4–L16.
42. Bajaj P, et al. (2011) Patterning the differentiation of C2C12 skeletal myoblasts. *Integr Biol (Camb)* 3(9):897–909.
43. Ahadian S, et al. (2013) Electrical stimulation as a biomimicry tool for regulating muscle cell behavior. *Organogenesis* 9(2):87–92.
44. Wehrle U, Düsterhöft S, Pette D (1994) Effects of chronic electrical stimulation on myosin heavy chain expression in satellite cell cultures derived from rat muscles of different fiber-type composition. *Differentiation* 58(1):37–46.
45. Hosseini V, et al. (2012) Engineered contractile skeletal muscle tissue on a micro-grooved methacrylated gelatin substrate. *Tissue Eng Part A* 18(23-24):2453–2465.
46. Flaibani M, et al. (2009) Muscle differentiation and myotubes alignment is influenced by micropatterned surfaces and exogenous electrical stimulation. *Tissue Eng Part A* 15(9):2447–2457.
47. Bian W, Juhas M, Pfeiler TW, Bursac N (2012) Local tissue geometry determines contractile force generation of engineered muscle networks. *Tissue Eng Part A* 18(9-10):957–967.
48. Dennis RG, Kosnik PE (2000) Excitability and isometric contractile properties of mammalian skeletal muscle constructs engineered in vitro. *In Vitro Cell Dev Biol Anim* 36(5):327–335.
49. Dennis RG, Kosnik PE, Gilbert ME, Faulkner JA (2001) Excitability and contractility of skeletal muscle engineered from primary cultures and cell lines. *Am J Physiol Cell Physiol* 280(2):C288–C295.
50. Bian W, Bursac N (2012) Soluble miniagrin enhances contractile function of engineered skeletal muscle. *FASEB J* 26(2):955–965.
51. Chan V, Zorlutuna P, Jeong JH, Kong H, Bashir R (2010) Three-dimensional photo-patterning of hydrogels using stereolithography for long-term cell encapsulation. *Lab Chip* 10(16):2062–2070.

Supporting Information

Cvetkovic et al. 10.1073/pnas.1401577111

SI Methods

Prepolymer Solutions. Prepolymer solution for bio-bots consisted of 20% (vol/vol) poly(ethylene glycol) diacrylate of M_r 700 g mol^{-1} (PEGDA M_r 700, Sigma-Aldrich) dissolved in PBS, with 0.5% (wt/vol) 1-[4-(2-hydroxyethoxy)phenyl]-2-hydroxy-2-methyl-1-propanone-1-one photoinitiator (Irgacure 2959, BASF) mixed from a 50% (wt/vol) stock solution in dimethyl sulfoxide (Fisher Scientific). Material properties and swelling ratio of this polymerized hydrogel have been previously characterized (1). Prepolymer solution for holders was made from 20% (wt/vol) poly (ethylene glycol) dimethacrylate of M_r 1,000 g mol^{-1} (Polysciences, Inc.) dissolved in PBS and mixed with 0.5% (wt/vol) Irgacure 2959.

Characterization of Working Curve and Control of Energy Dose. After the stereolithography apparatus (SLA) polymerizes the first layer of a part, the stage moves down a distance that is equal to the height of the first layer, the surface is recoated with prepolymer solution, the laser power is recalibrated, and the second layer is polymerized. This "bottom-up" assembly process continues until the entire part is built. Because the SLA fabricates a part in multiple steps, layers can be produced with different materials or properties. Following a well-characterized working curve equation (2, 3), which quantifies the relationship between maximum exposure (polymerization energy) and thickness of the fabricated layer, we varied two parameters that control the polymerization energy of the SLA (laser penetration depth into the material and critical energy dose needed to polymerize the material from a liquid to a solid gel state) to obtain bio-bots with varying beam stiffness and bending profiles (Fig. S2).

The working curve equation is derived from the Beer–Lambert law, which describes the intensity of light's exponential decay as it travels through an absorbing medium. The equation quantifies the relationship between the maximum exposure (E_{max}), the critical energy dose needed to polymerize the material from a liquid to a solid gel state (E_C), the thickness or cure depth (C_D), and the penetration depth (D_P) of the laser into the material (2).

$$C_D = D_P \cdot \ln\left(\frac{E_{max}}{E_C}\right). \quad \text{[S1]}$$

Cylinders with a radius of 1 cm and a height of 100 μm were fabricated from PEGDA M_r 700 with 0.2-μm Nile Red fluorescent microbeads (Spherotech) encapsulated in a 1:500 ratio of beads to polymer. E_{max} was varied from 71 to 512 mJ cm^{-2} by maintaining a constant E_C value and changing the input D_P value. The thicknesses of the fabricated parts (C_D) were measured using an inverted fluorescent microscope with a tetramethylrhodamine excitation filter. The beads encapsulated in the bottommost plane of the cylinder were brought into focus and this location was set as zero. The focus was then set on the topmost plane of encapsulated beads in the cylinder and this change in displacement was recorded as the height of the cylinder. Four parts were fabricated for each energy dose and an average height was taken from four points per part. The average thickness was plotted against the applied energy dose and a logarithmic trendline was fit to the data to create a working curve (Fig. S2C). As described in the text, the energy dose of the laser was altered by inputting values of D_P and E_C to polymerize with a certain E_{max}. The hydrogel's stiffness varied logarithmically with E_{max}.

Cell Culture. Cells were maintained in growth medium (GM) consisting of Dulbecco's Modified Eagle Medium with L-glutamine and sodium pyruvate (DMEM, Corning Cellgro), supplemented with 10% FBS (Lonza), 1% penicillin-streptomycin, and 1% L-glutamine (both Cellgro Mediatech, Inc.). Differentiation medium (DM) consisted of DMEM supplemented with 10% horse serum (HS, Lonza), 1% penicillin-streptomycin, and 1% L-glutamine.

Components of Collagen- and Fibrin-Based Muscle Strips. Before cell seeding, bio-bots were positioned beam-down in polymerized holders in a 35-mm cell culture dish and aspirated of excess liquid. For collagen muscle strips, an ice-cold cell–matrix solution of Matrigel basement membrane matrix (30% of total cell–matrix volume, BD Biosciences), liquid type I collagen (1.4 mg ml^{-1}, BD Biosciences) neutralized with NaOH (0.01 N), and C2C12s of densities varying from 1–10 × 10^6 cells ml^{-1} suspended GM (at a volume equal to that of collagen) were added to each holder in a total volume of 100 μL. For fibrin muscle strips, an ice-cold cell–matrix solution of Matrigel (30% of total cell–matrix volume), fibrinogen (4 mg ml^{-1}, Sigma-Aldrich), thrombin from bovine plasma [0.5 U (mg fibrinogen)$^{-1}$, Sigma-Aldrich], and C2C12s suspended in GM at a concentration of 5 × 10^6 cells ml^{-1} were added to each holder in a total volume of 120 μL unless otherwise specified. After 1 h, 4 mL of GM was added. After 24 h, bio-bots were released from holders and switched to DM. All cells and bio-bots were maintained at 37 °C and 5% CO$_2$, with daily media changes.

Mechanical Testing. Dogbone-shaped test specimens (PEGDA M_r 700) were fabricated with the same thickness as that of the beam and with energy doses ranging from 105–513 mJ cm^{-2}. Specimens were fixed in a hydrated 37 °C sample chamber filled with PBS using custom-fabricated structures subjected to tensile loading. A video extensometer tracked the displacement of four points on the sample until fracture, which was used to calculate elastic modulus for different polymerization energy doses (Fig. S5B). Elastic modulus E was determined from the linear portion of stress–strain curves according to Hooke's law ($\sigma = \varepsilon E = F/A$), assuming a slow strain rate. Moduli of energy doses not measured were extrapolated from a best-fit curve. Cross-sectional area was measured with calipers.

Calculation of Compaction Area. To measure the cross-sectional compaction area, holders containing the bio-bots seeded with 90 μL of cell–matrix suspension were imaged at 0.8× using a stereoscope with a digital microscope camera at 1, 6, 12, and 24 h after cell seeding (Fig. S2D). The Measure tool in ImageJ was used to calculate the cross-sectional area by quantifying the visible compacted area of the cell–matrix solution and subtracting the cross-sectional area of the pillars.

Study of Beam Stiffness and Bending. Bio-bots structures were polymerized with varying energy doses from 109–512 mJ cm^{-2}. The cell density was kept constant at 1 × 10^6 cells ml^{-1} and bio-bots were cultured in GM with 10% FBS. Images were acquired daily using a stereoscope with a digital microscope camera (Fig. S5A).

Calculation of Passive Tension. Passive tension in the muscle strip at rest was determined using Euler–Bernoulli linear beam theory relating deflection of a curved beam to an applied moment. Assuming negligible rotation in the beam and a small angle

approximation, equating the applied moment M to tension P times the moment arm l from the muscle strip to the beam reduced the second-order differential equation to

$$\frac{d^2 y}{dx^2} = \frac{M}{EI},$$ [S2]

where I is the moment of inertia of the rectangular cross-section and y is the horizontal deflection of the beam. Boundary conditions were applied by assuming zero deflection at ends of the beam ($L = 0$) and maximum deflection δ_{max} at the center ($L/2$).

$$\delta_{max} = |y(L/2)| = \frac{ML^2}{8EI} = \frac{PlL^2}{8EI}.$$ [S3]

Beam dimensions, moment arm, and maximum deflection were averaged from three measurements of each device using the Measure Tool in ImageJ (National Institutes of Health). Solving for P yielded the relation

$$P = \frac{8EI\delta_{max}}{l\,L^2}.$$ [S4]

To verify the accuracy of the calculation method, the computed passive tension values were input into ANSYS (finite-element software), and the simulation produced values for deflection of the beam (Fig. S5D).

Electrical Stimulation Setup. To create the electrical stimulation setup, the output from a waveform generator was amplified through an AD797 inverting amplifier. A capacitor C was added in series to minimize electrolysis of the media by converting the square pulse to a biphasic pulse; the system was then treated as an RC circuit (Fig. S6A). A 35-mm culture dish was modified to allow Pt electrodes of diameter 0.762 mm to pass through the lid of the dish (4). The average resistance of the electrical stimulation medium (DMEM without serum) was calculated by measuring the time constant τ from the oscilloscope and dividing by C for each volume at 23 °C and 37 °C. The conductivity of the medium was measured using a pH–conductivity meter (Orion 4-Star, Thermo Scientific), at 23 °C and 37 °C (Fig. S6B). During stimulation, the bio-bot was placed in 4 mL of warm electrical stimulation medium between the positive and ground electrodes and a current was applied perpendicular to the long axis, with stimulation frequencies up to 10 Hz and never exceeding more than half of the sampling frequency, as per the Nyquist criterion. Simultaneous imaging was achieved by positioning the dish on the stage of a stereoscope (Fig. S6 D and E).

Active Tension. Active tension exerted by contracting muscle strips upon electrical stimulation was calculated by treating the bio-bot structure as a viscoelastic body governed by a Kelvin–Voigt model:

$$\sigma(t) = E\varepsilon(t) + \eta\frac{d\varepsilon(t)}{dt}.$$ [S5]

The active stress generated by the muscle strip was computed as a function of the strain $\varepsilon(t)$ and strain rate $[d\varepsilon(t)]/dt$ observed in the hydrogel beam with viscosity η. The time-varying displacement data were converted into time-varying strain and Eq. S5 was used to compute the resulting active stress.

Simulation of Locomotion. To model deformation and stress in the active (contracting) state, pillar displacements (from the MATLAB script) were imported into the simulation to recapitulate the walking motion captured from top-view movies of symmetric and asymmetric bio-bots. Bio-bots were placed on a frictionless support surface ("ground") and allowed to deform and move with respect

to the ground in response to the displacement input. The simulation provided time-varying stresses in the bio-bot structure and time-varying reaction forces from the ground.

Calculation of Relative Pillar Displacement. To find the time-averaged ratios of pillar movement, the difference in X and Y coordinates of the pillar caps for each point was converted to a total distance moved between individual frames (i.e., from n to $n+1$), then divided.

$$\frac{pillar_1}{pillar_2} = \frac{\sqrt{(\Delta x_{p1})^2 + (\Delta y_{p1})^2}}{\sqrt{(\Delta x_{p2})^2 + (\Delta y_{p2})^2}}$$

$$= \frac{\sqrt{(x_{p1(n+1)} - x_{p1(n)})^2 + (y_{p1(n+1)} - y_{p1(n)})^2}}{\sqrt{(x_{p2(n+1)} - x_{p2(n)})^2 + (y_{p2(n+1)} - y_{p2(n)})^2}}.$$ [S6]

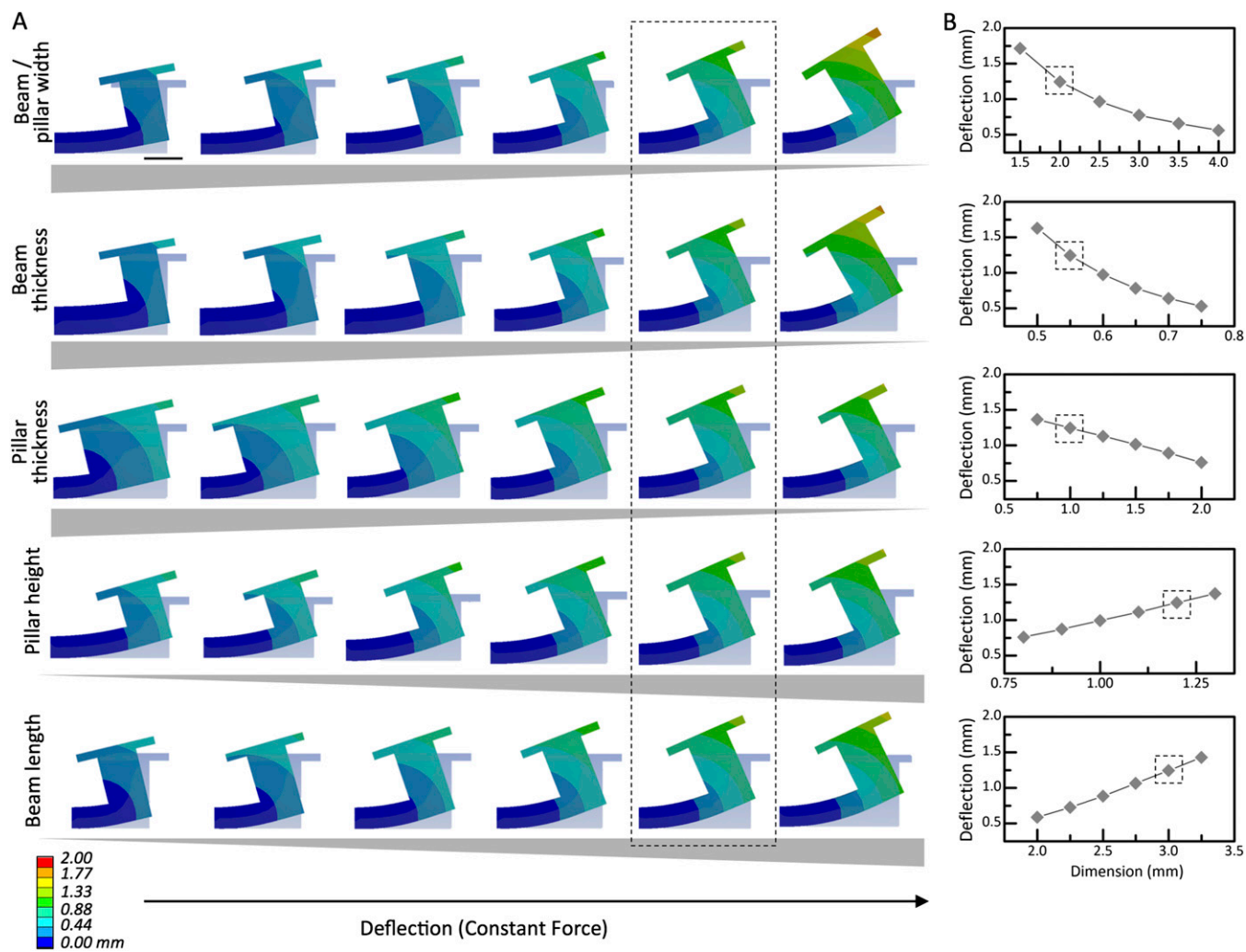The difference in X and Y position between two consecutive frames is shown for one pillar in Fig. S8E.

Immunofluorescence and Histology. Bio-bot pillars were cut to allow for muscle strip isolation and removal. Tissues were rinsed in PBS, fixed in 4% (vol/vol) paraformaldehyde, and permeabilized with 0.2% (vol/vol) Triton X-100 (Sigma-Aldrich) for 5–10 min. Image-iT FX Signal Enhancer (Invitrogen) was added for 30 min. Tissues were first incubated with mouse MF-20 antimyosin heavy chain (1:400, Developmental Studies Hybridoma Bank, The University of Iowa Department of Biology) and rabbit sarcomeric α-actinin (1:600, Abcam) primary antibodies in Image-iT FX Signal Enhancer (Invitrogen) for 2 h at room temperature (fibrin muscle strips) or overnight at 4 °C (collagen muscle strips) and washed with PBS. Fibrin muscle strips were incubated with Alexa Fluor 488 goat anti-mouse IgG and Alexa Fluor 568 F(ab′)₂ fragment of goat anti-rabbit IgG secondary antibodies (1:400, Invitrogen) in Image-iT FX for 2 h in the dark. Collagen tissues were incubated with Alexa Fluor 594 goat anti-rabbit and Alexa Fluor 488 goat anti-mouse secondary antibodies for 2 h. Next, 4′,6-diamindino-2-phenylindole (DAPI, 1:5,000 in sterilized deionized water, Sigma-Aldrich) was added for 5–10 min in the dark. Muscle strips were fixed to a 35-mm glass-bottom microwell dish (MatTek) with warm agarose gel.

For histological staining, muscle strips were fixed for a minimum of 12 h in 70% EtOH, then dehydrated and fixed in an overnight tissue processor (ASP300, Leica). Samples were embedded in paraffin, cut into 5–15-μm sections with a microtome (Leica), mounted on glass slides, and stained with hematoxylin and eosin (H&E). After 24 h, they were imaged with a digital pathology system (Nanozoomer). For quantification of cell distribution, a threshold was applied to each H&E image to distinguish nuclei from background. The ImageJ Analyze Particles feature was used to determine X–Y coordinates of each nucleus on every image, and the minimum distance of each nucleus to the perimeter was calculated.

Cell Viability Assay. Muscle strips containing 5×10^{-6} cells ml^{-1} and supplemented with insulin-like growth factor 1 (IGF-1) and aminocaproic acid (ACA) were incubated with MTS ([3-(4,5-dimethylthiazol-2-yl)-5-(3-carboxymethoxyphenyl)-2-(4-sulfophenyl)-2H-tetrazolium, Promega) and phenazine methosulfate (Sigma-Aldrich) in DMEM without phenol red for 4 h at 37 °C and 5% CO_2. Absorbance of MTS formazan product formation was measured at 490 nm using a Synergy HT microplate reader (BioTek) for four different time points ($n = 4$ each) and normalized to day 0 (day of cell seeding). The absorbance was assumed to be directly related to the quantity of living cells.

Statistical analysis. Results are presented as mean ± SD. All statistical analyses were performed with OriginPro software and represent one-way ANOVA followed by Tukey's Multiple Comparison Test for $P < 0.001$, $P < 0.01$, or $P < 0.05$ as noted.

1. Chan V, Zorlutuna P, Jeong JH, Kong H, Bashir R (2010) Three-dimensional photopatterning of hydrogels using stereolithography for long-term cell encapsulation. *Lab Chip* 10(16): 2062–2070.
2. Jacobs PF (1992) *Rapid Prototyping and Manufacturing: Fundamentals of StereoLithography*, ed Reid DT (Society of Manufacturing Engineers, Dearborn, MI), 1st Ed.
3. Arcaute K, Mann BK, Wicker RB (2006) Stereolithography of three-dimensional bioactive poly(ethylene glycol) constructs with encapsulated cells. *Ann Biomed Eng* 34(9):1429–1441.
4. Bajaj P, et al. (2011) Patterning the differentiation of C2C12 skeletal myoblasts. *Integr Biol (Camb)* 3(9):897–909.

Fig. S1. Bio-bot development and timeline. (*A*) Flowchart of design and optimization parameters, including structural design, material properties, ECM microenvironment, and conditions of cell seeding and culture. (*B*) A timeline representing the development of a functional bio-bot.

Fig. S2. Linear elastic simulation of PEGDA hydrogel bio-bot deflection with varying dimensions. The deflection was simulated using ANSYS in response to a constant passive tension force of 992.7 µN (corresponding to a beam of modulus 319.4 kPa). Bio-bot design dimensions were optimized to maximize deflection and reduce scaffold weight, while preserving ease of manipulation during experimentation and electrical stimulation. The optimal design (column highlighted by a dotted box), therefore, was chosen for its ability to combine high deflection with a robust mechanical structure. Shown are structures with global deflection (*A*) and plots of deflection versus varied dimensions (*B*), including beam–pillar width, beam thickness, pillar thickness, pillar height, and beam length. Optimal dimensions are indicated by a dotted box on the plots. Scale bar, 1 mm.
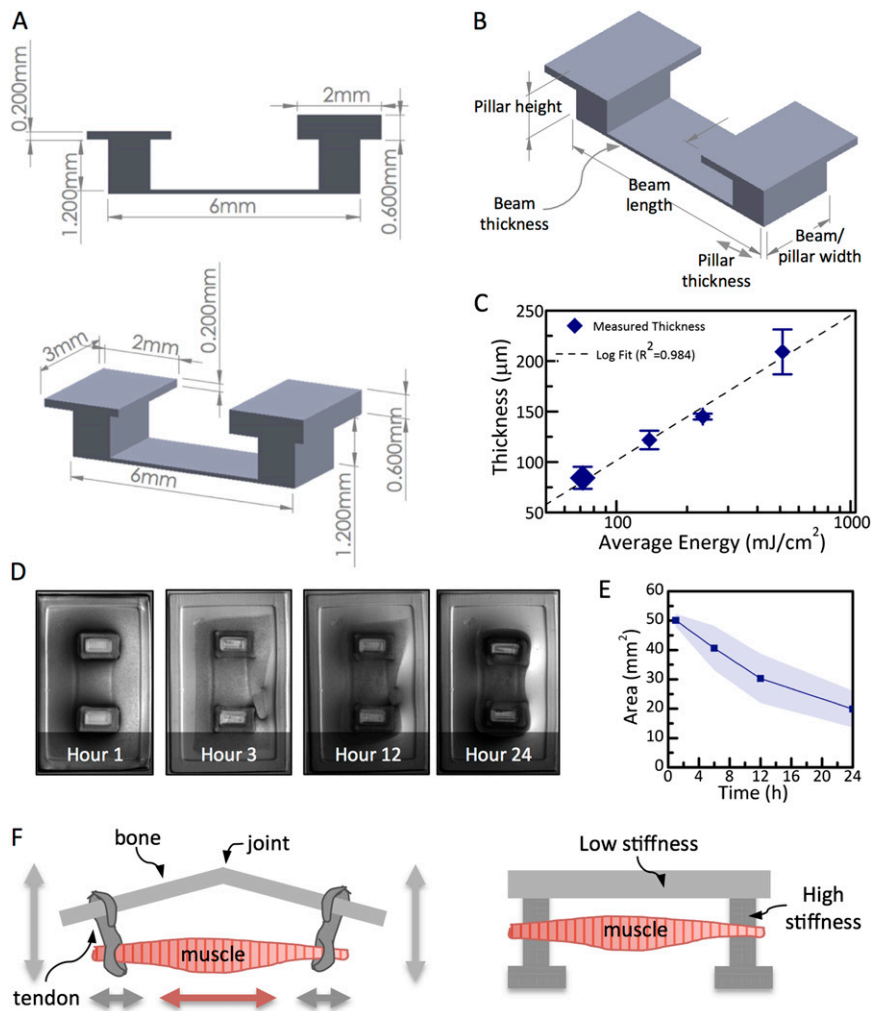
Fig. S3. Bio-bot design and fabrication. SolidWorks parts and dimensions of the bio-bot are shown. (*A*) The asymmetric design for the walking bio-bot had a taller cap at the end of the pillar and is shown from top-angled and side views. (*B*) Parameters from Fig. S2 are assigned to bio-bot dimensions. (*C*) A working curve for PEGDA M_r 700 correlates the energy dose from the SLA laser with the polymerized layer thickness. (*D*) Time-lapse compaction of cell–matrix solution with IGF-1. During the 24–48 h after seeding, the liquid suspension of cells and fibrin–Matrigel matrix polymerized and condensed around the pillars to form a solid muscle strip (top view). Skeletal myoblasts embedded in extracellular matrix proteins were induced to differentiate and self-assemble into 3D muscle strips anchored at both ends, an arrangement which facilitated cell growth, spreading, and differentiation in a supportive and constrained environment. (*E*) Cross-sectional compaction area of muscle strips decreased over the first 24 h due to compaction of the matrix and the exertion of traction forces from the cells ($n = 20$). Data are presented as mean $\pm$ SD (shaded region). (*F*) Schematic of a physiological muscle–tendon–bone architecture, in which force transmission occurs from a contracting muscle to bone through a connecting tendon (*Left*), as the inspiration for the basic design of our bioactuator (*Right*).
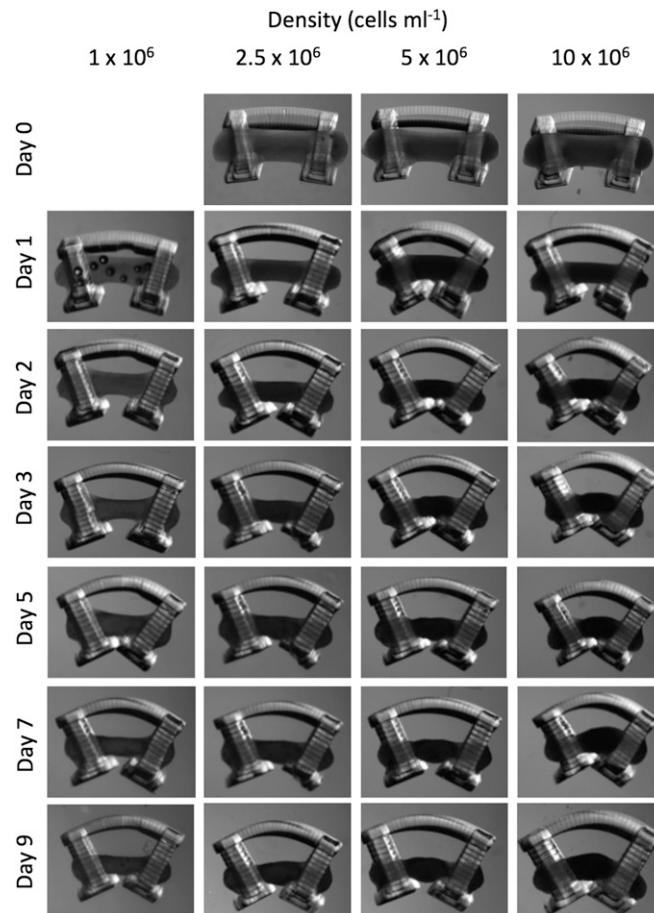
Fig. S4. Effect of cell density on bio-bot bending with constant modulus. Bio-bots structured fabricated with 138-mJ cm^{-2} energy dose were seeded with collagen-based cell–matrix solutions with varying cell densities (1–10 × 10^6 cells ml^{-1}) in growth medium. After 72 h, DM with 1 mg ml^{-1} ACA was added.
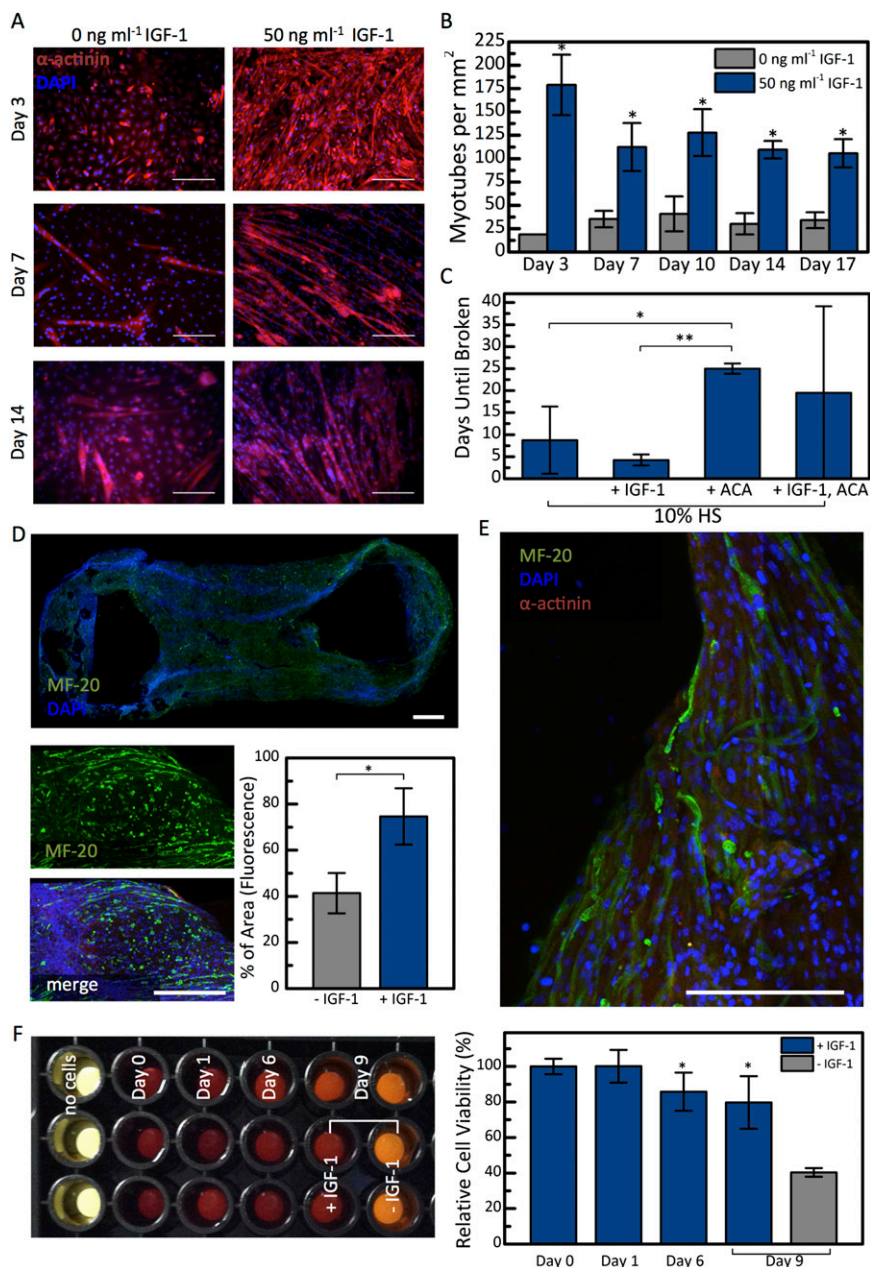
Fig. S5. Muscle strip formation, viability, and differentiation. (*A*) Fluorescent images demonstrating the differentiation and maturation of myotubes over time with the addition of 50 ng ml^{-1} IGF-1 to differentiation medium containing 2% HS. Scale bar, 100 μm. (*B*) The myotube density was significantly increased for each time point after day 3 with the addition of IGF-1 compared with the control (*n* = 3). Fusion of multinucleated myotubes with additional myoblasts during myogenic differentiation explains the decrease in density between days 3 and 7. Non–IGF-1–supplemented samples displayed an average myotube density of 11 ± 0 myotubes mm^2 on day 3, which explains the lack of error bar at this time point. (*C*) The lifetime of the fibrin bio-bots (i.e., days until fracture of the muscle strip) was characterized by culture in differentiation medium in the presence or absence of 50 ng ml^{-1} IGF-1 and/or 1 mg ml^{-1} ACA. We noted a significant increase in the muscle strip lifetime compared with the control of 10% HS (from 8.75 ± 7.63–25 ± 1.15 d; *P* < 0.01, *n* = 4) with the addition of 1 mg ml^{-1} ACA. The addition of 50 ng ml^{-1} IGF-1 decreased the number of days until fracture compared with the control (51.43% decrease) and 1 mg ml^{-1} ACA condition (22.0% decrease). (*D*) A longitudinal slice (−IGF-1) and region of the fibrin muscle strip with immunostaining of antimyosin heavy chain MF-20 and DAPI staining contained myoblasts and myotubes. Scale bars, 500 μm. Fluorescence analysis demonstrated a significantly higher portion of cells in muscle strip sections (as indicated by percentage of MF-20 fluorescence area, representing skeletal muscle cells) with the addition of IGF-1 (74.7 ± 12.2%, *n* = 7) compared with no IGF-1 treatment (41.4 ± 8.7%, *n* = 4). For *B–D*, statistics represent one-way ANOVA and Tukey's *test*, with * = *P* < 0.01 and ** = *P* < 0.001. (*E*) Multinucleated myotubes were aligned along the perimeter of the fibrin muscle strip (+IGF-1). Scale bar, 200 μm. (*F*) Relative absorbance, indicative of viability of cells within the muscle strip at various time points from day 0 (day of cell seeding) to day 9 (day of electrical stimulation). Statistical significance was not calculated between +IGF-1 and −IGF-1 samples on day 9, because differences in cell density (resulting from addition of IGF-1) can lead to differences in absorbance values. The image at left demonstrates a qualitative difference in formazan product formation. For all charts, values are presented as mean ± SD. For *F*, statistics represent one-way ANOVA and Tukey's *test*, with * = *P* < 0.05.
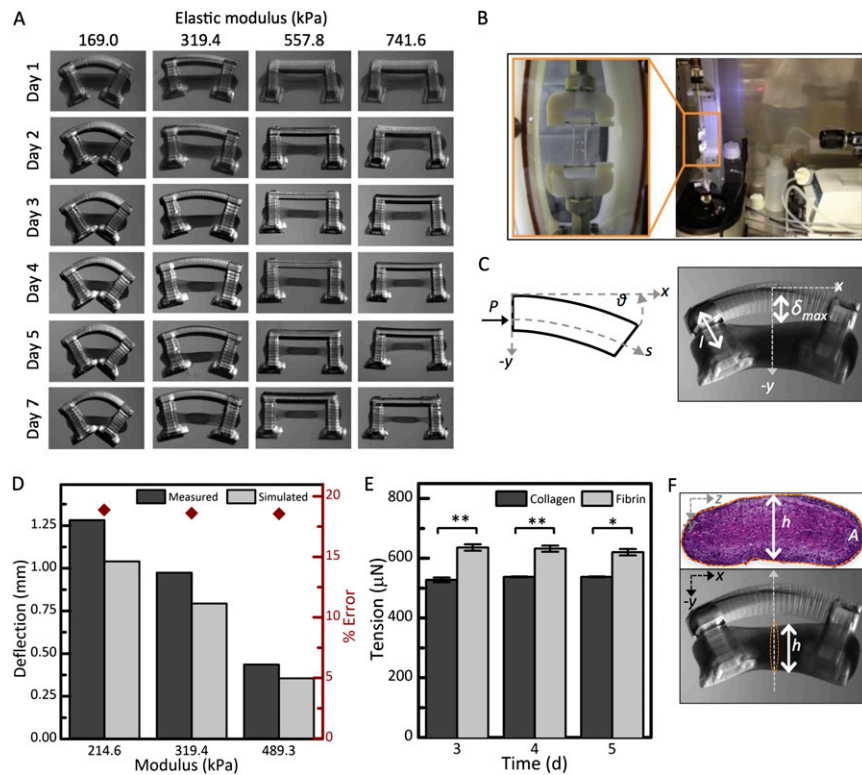
Fig. S6. Mechanical characterization of stiffness, tension, and stress. (*A*) Effect of beam stiffness on collagen bio-bot bending. The bending in the stiffer beams was negligible in comparison with those with lower elastic moduli, and could not support net displacement of the bio-bot. (*B*) Setup of hydrated tensile testing chamber. (*C*) Schematic showing beam in compression undergoing nonlinear bending. The midpoint of the beam is set as the origin. δ_{max} is the maximum deflection of the beam and *l* is the moment arm from the muscle strip to the beam. (*D*) The measured and simulated values of maximum beam deflection recorded for bio-bots of various energy doses on day 8. To verify the accuracy of the calculation method, the computed passive tension values were input into ANSYS, and the simulation produced values for deflection of the beam. The error between the actual and simulated values was calculated as ~18% for the three bio-bots, validating the use of linear bending theory to predict the force in the muscle strip. (*E*) Fibrin muscle strips exhibited 17.8% higher passive tension, on average (*n* = 6 for days 3 and 4; *n* = 2 for day 5), compared with collagen muscle strips (*n* = 2) over the time period shown for 1×10^6 cells ml^{-1} density. Statistics represent one-way ANOVA and Tukey's *test*, with * = $P < 0.01$ and ** = $P < 0.001$. (*F*) Transverse histological cross-sections were used to calculate the cross-sectional area of the muscle strips for calculation of stresses.
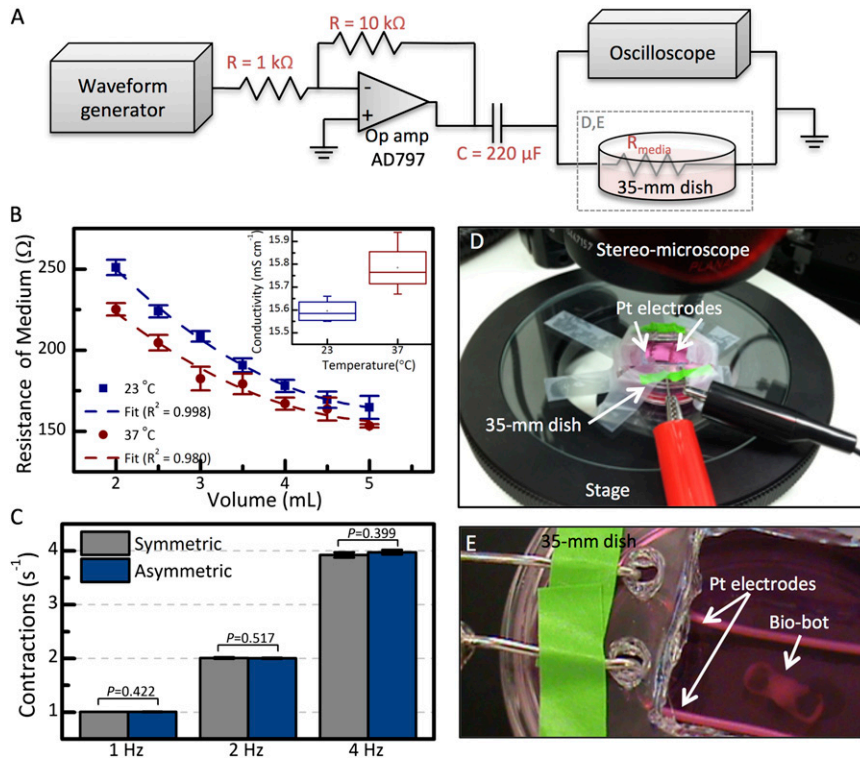
Fig. S7. Electrical stimulation setup and characterization. (*A*) Schematic of custom-built electrical stimulation setup. (*B*) Average resistance (*n* = 3) and conductivity (*Inset, n* = 4) of the electrical stimulation medium (DMEM without serum) at 23 °C and 37 °C. Boxes represent 25th, 50th, and 75th percentile; • represents mean value; whiskers represent minimum–maximum values. (*C*) Average number of contractions per second of electrically stimulated bio-bots, measured over a stimulation period of 130 s (*n* = 5 for each condition). The introduction of asymmetry into the design did not significantly alter the response to stimulation. (*D* and *E*) Stimulation and imaging setup. In most cases, net movement was observed with electrical stimulation multiple times per day over consecutive days, without significant adverse effects.
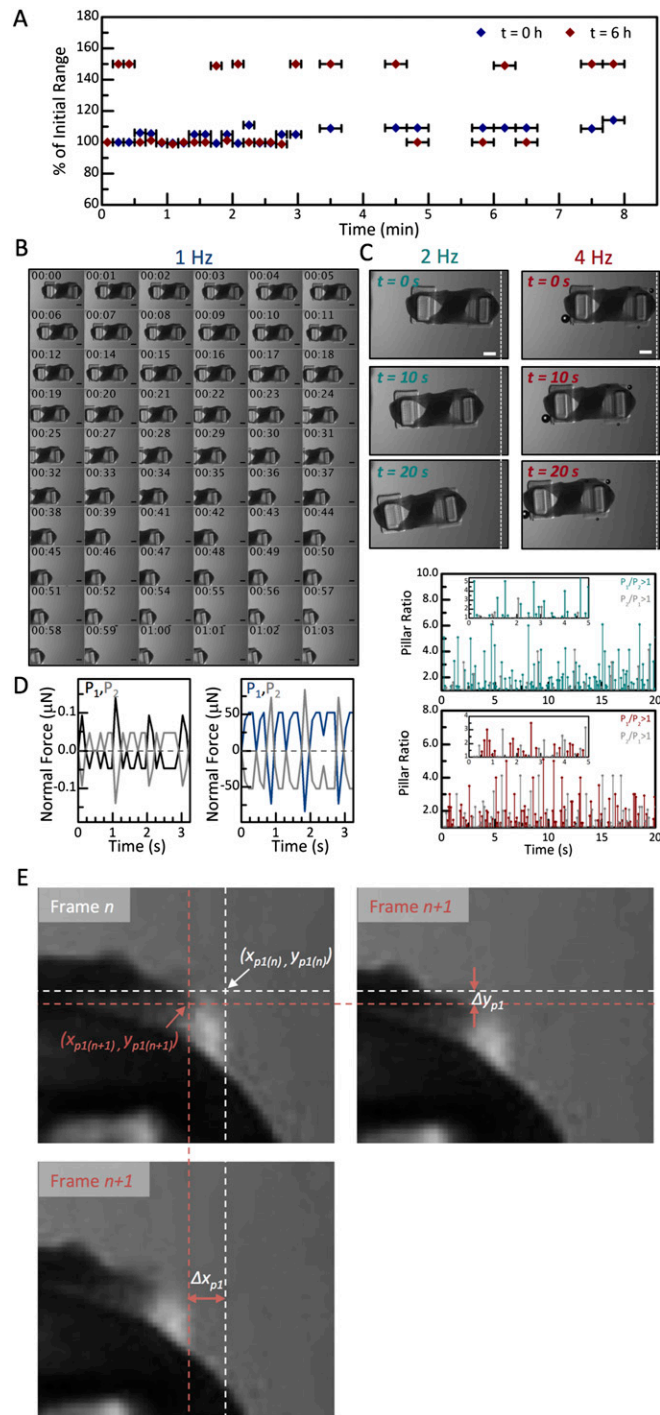
Fig. S8. Characterization of bio-bot movement at various stimulation frequencies. (*A*) Over 8 min, the range of active tension remained between 99.3% and 111.0% of the initial tension (i.e., the first time point of 0–10 s) for hour 0, and between 98.8% and 150% for hour 6 of the same bio-bot. (*B*) Top-view time-lapse montage (1-s increments) showing the movement and net displacement of the bio-bot characterized in Fig. 5 with electrical stimulation at 1 Hz. Scale bar, 1 mm. (*C*) Top-view time-lapse images of the movement of the bio-bot characterized in Fig. 5 with electrical stimulation at 2 Hz (*Left*) and 4 Hz (*Right*). Examination of top-view movies revealed the relative range of motion of each pillar during contraction, which dictated the degree of net displacement. The direction of net displacement corresponded to that of the pillar with a greater average range of motion (ratio > 1). (*D*) Normal forces are shown for a symmetric (*Left*) and asymmetric (*Right*) bio-bot, shown over a time period of 3 s (three contractions at 1-Hz stimulation). Directional movement occurred when discrepancies in coefficients of friction between the pillars and the ground, resulting from a phase delay in the spatially varying contractile response of the muscle strip in response to electrical stimulation, caused one to "stick" and the other to "slide" with respect to the surface. (*E*) Calculation method to determine time-averaged ratios of relative pillar displacement. The difference in X and Y position between two consecutive frames is shown for one pillar in this figure. The unequal range of motion between the pillars was attributed to two causes: first, variability in cell–matrix compaction which led to uneven moment arms in the two pillars, causing uneven bending in the beam and hence unequal pillar displacements; and second, time-varying normal reaction forces and therefore time-varying frictional forces that restricted the range of motion of each pillar, due to an imbalanced distribution of mass within the muscle strip that caused the weight assumed by each pillar to vary during movement.
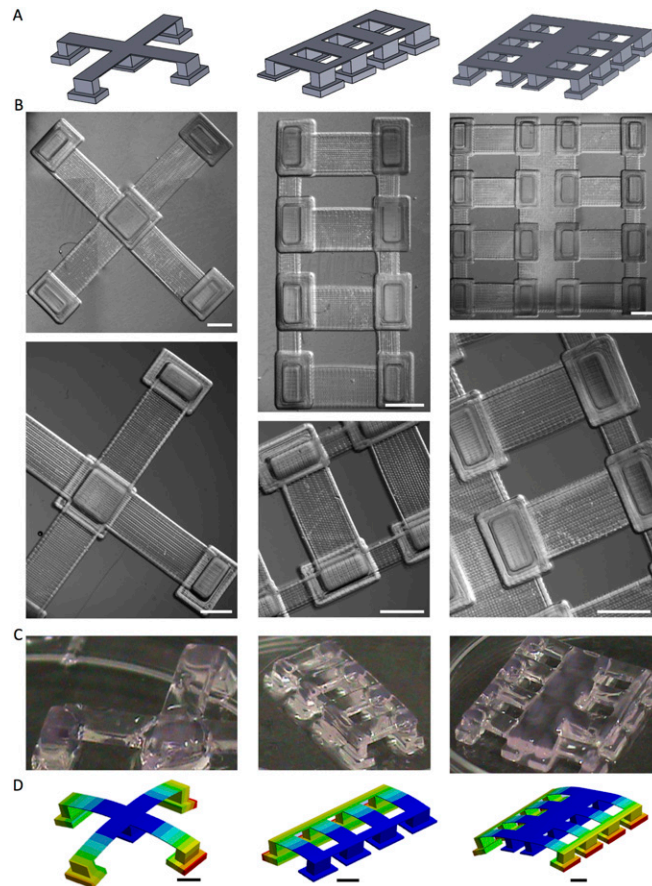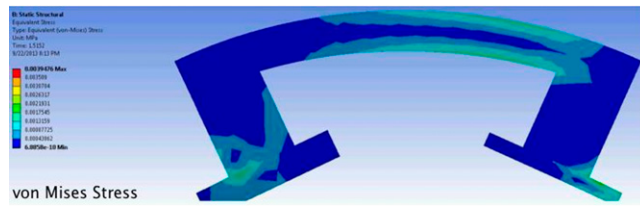
Fig. S9. Design, fabrication, and simulation of multilegged designs. Due to a fabrication technology offering a great deal of flexibility in specifying geometric and design parameters, the designs presented in the main figures were adapted to demonstrate the ability to build machines with varying number and arrangement of pillars. Images of computer-aided designs (*A*), fabricated hydrogel machines (top views, *B,* and side angled views, *C*), and finite-element analysis simulations of deflections (*D*) are shown for three different designs. Scale bars, 2 mm.
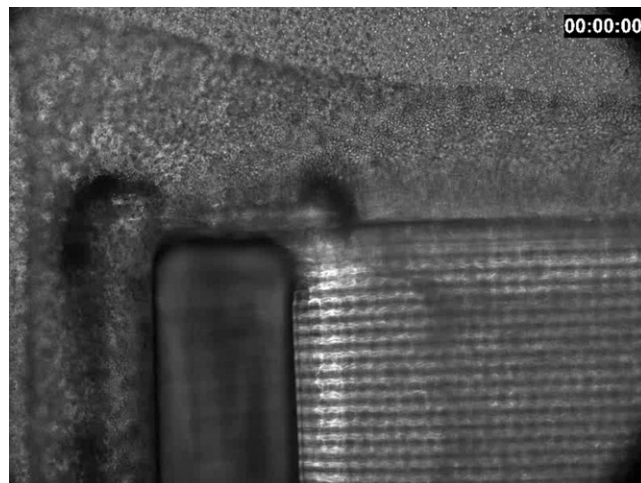
Movie S1. Compaction of muscle strip. Time-lapse visualization of fibrin gel compaction during the first 12 h following cell seeding. Seeding conditions included: 138-mJ cm^{-2} energy dose, 5×10^6 cells ml^{-1}, 4 mg ml^{-1} fibrinogen, 1 mg ml^{-1} ACA, and 50 ng ml^{-1} IGF-1.

[Movie S1](#)

Movie S2. Control of pacing with electrical stimulation. Top-view movie of bio-bot paced at increasing stimulation frequencies (1, 2, 3 Hz). The muscle strip contracted with enough force to move the pillars of the structure.

[Movie S2](#)

Movie S3. Side-view movement. Side-view movie of an asymmetric bio-bot at 1 Hz, 2 Hz (with corresponding top-view movie), and 4 Hz over time.

[Movie S3](#)

Movie S4. Simulation of reaction forces from ground to pillars and von Mises equivalent stresses in a symmetric bio-bot.
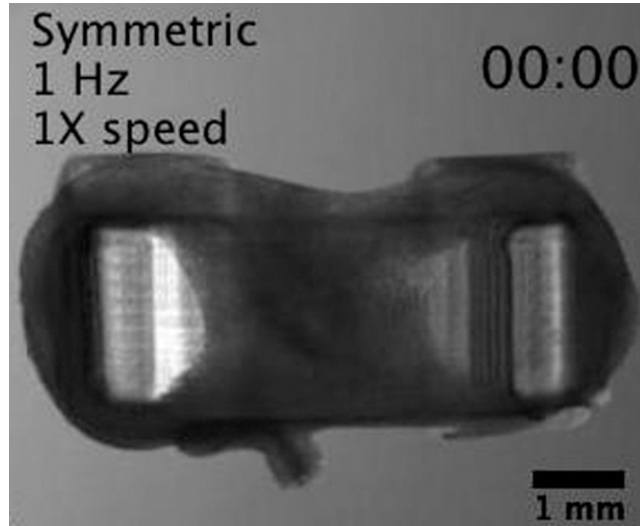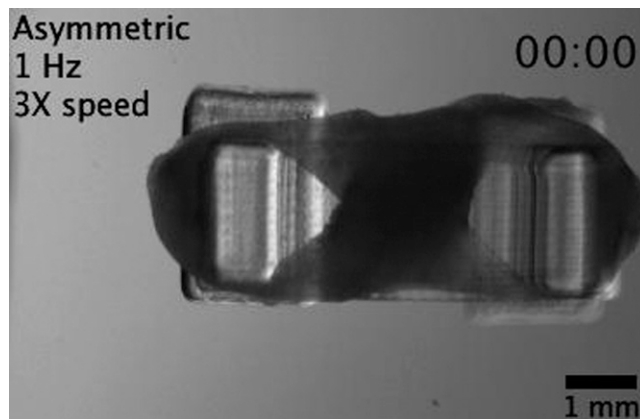
[Movie S4](#)

Movie S5. Simulation of reaction forces from ground to pillars and von Mises equivalent stresses in an asymmetric bio-bot.
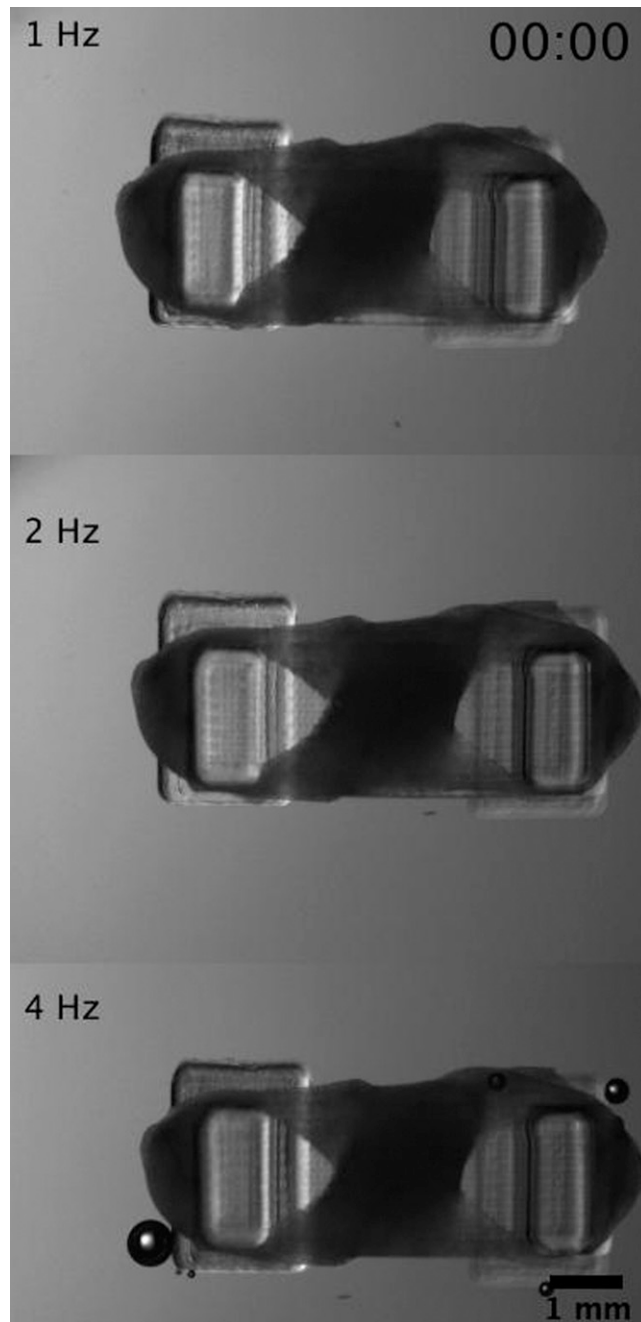
Movie S5

Movie S6. Symmetric bio-bot movement at 1 Hz. Top-view movie demonstrating the net movement of a symmetric bio-bot at 1 Hz (1× speed). Scale bar, 1 mm.

Movie S6

Movie S7. Asymmetric bio-bot movement at 1 Hz. Top-view movie demonstrating the net movement of an asymmetric bio-bot at 1 Hz (3× speed). Scale bar, 1 mm.

Movie S7

Movie S8. Asymmetric bio-bot movement at various frequencies. Top-view movie comparing the contraction and movement of an asymmetric bio-bot at 1, 2, and 4 Hz over the course of 10 s. Scale bar, 1 mm.

[Movie S8](#)